Luminescence, Chemical Sensing and Mechanical Properties of Crystalline Materials Based on Lanthanide–Sulfonate Coordination Polymers

Article *in* RSC Advances · November 2016

DOI: 10.1039/C6RA23516F

CITATIONS
10

READS
159

6 authors, including:

Richard Fernando D'vries
Universidad Santiago de Cali
56 PUBLICATIONS **374** CITATIONS
SEE PROFILE

German E. Gomez
Karlsruhe Institute of Technology
26 PUBLICATIONS **98** CITATIONS
SEE PROFILE

Diego Fernando Lionello
Comisión Nacional de Energía Atómica
9 PUBLICATIONS **17** CITATIONS
SEE PROFILE

Maria Cecilia Fuertes
Comisión Nacional de Energía Atómica
45 PUBLICATIONS **781** CITATIONS
SEE PROFILE

RSC Advances

Accepted Manuscript

This article can be cited before page numbers have been issued, to do this please use: R. F. D'Vries, G. Gómez, D. E. Lionello, C. Fuertes, G. Soler-Illia and J. A. Ellena, *RSC Adv.*, 2016, DOI: 10.1039/C6RA23516F.

ROYAL SOCIETY OF CHEMISTRY

rsc.li/rsc-advances

View Article Online
DOI: 10.1039/C6RA23516F

Journal Name

ARTICLE

Luminescence, Chemical Sensing and Mechanical Properties of Crystalline Materials Based on Lanthanide-Sulfonate Coordination Polymers.†

Received 00th January 20xx,
Accepted 00th January 20xx

DOI: 10.1039/x0xx00000x

www.rsc.org/

Richard F. D'Vries,[a]* German E. Gomez,[b]* Diego F. Lionello,[b] M. Cecilia Fuertes,[b] Galo J. A. A. Soler-Illia,[c] Javier Ellena.[a]

Lanthanide-coordination polymers (Ln-CPs) constitute relevant compounds for the design of multifunctional materials. Nevertheless, studies devoted to understand relationships of combined structural-optical-mechanical properties are scarcely reported. In this work, an exhaustive study of a series of CPs obtained from lanthanide metals, 3-hydroxinaphthalene-2,7-disulfonate(3-OHNDS) and 1,10-phenanthroline (phen) as ligands is presented. Two crystalline phases were identified with general formula $[Eu(3\text{-}OHNDS)(Phen)(H_2O)_2]\cdot 3H_2O$ (**Phase 1-Eu**), and $[Ln_2(3\text{-}OHNDS)_2(Phen)_2(H_2O)]\cdot 3H_2O$ (**Phase 2-Ln**), where Ln^{3+} = Tb, Dy, Ho, Er and Yb. Both phases were characterized by powder and single crystal X-ray diffraction, vibrational and thermal analysis and scanning electron microscopy. Moreover, nanoindentation analysis was performed in order to find relationships between structural features and the mechanical properties of the crystalline materials. The photoluminescence (PL) properties of the reported phases were also explored, involving excitation-emission experiments and quantification of color emission. Finally, one compound was selected as chemical sensor model, exhibiting different optical behaviour in the prescence of aromatic molecules, principally towards naphtalene molecules. These results make these compounds promising materials for the elaboration of selective chemical sensors.

Introduction

In the exploration of synthesis methodologies to obtain new crystalline materials such as coordination polymers (CPs) and metal-organic frameworks (MOFs), different procedures applying the principles of crystal engineering has been developed.[1, 2] However, it is hard to find systematic paths addressed to elucidate synthetic mechanism and related structural features with physical, chemical or electronic properties.

From the synthetic point of view, the use of polytopic linkers increases the possibility to obtain multiple structural phases. It provides an excellent scenario to make studies about synthesis, structure and its properties.

In this context, sulfonate linkers represent new opportunities to explore the synthesis of CPs, due to the versatility to form covalent bonds and hydrogen interactions.[3] Recent works have demonstrated that under hydro or solvothermal conditions the sulfonate group increases its coordination ability, improving its capacity to form compounds with different architectures, dimensionalities and topologies.[4, 5] These different structural features have a high impact in resulting properties as catalysis,[6, 7] gas absorption,[8, 9] luminescence,[4, 10, 11] magnetism and conductivity.[12, 13] Our research is focused on the understanding of the sulfonate group behavior under hydrothermal conditions as well as the formation equilibrium involved in the reaction.[14, 15] In this work we choose two aromatic π-conjugated linkers (3-OHNDS and 1,10-phenanthroline) and lanthanides as building blocks for the construction of optically active platforms. It is known that lanthanide ions present rich optical features derived from intra-configurational 4f-4f transitions, being some of them of *hypersensitive* nature.[16] This key property is important for sensing applications,[17] which is a field in exponential growth.

[a] *Instituto de Física de São Carlos, Universidade de São Paulo, CP. 369, 13560-970, São Carlos - SP, Brasil.*
[b] *Gerencia de Química, Centro Atómico Constituyentes, Comisión Nacional de Energía Atómica (CAC-CNEA), Av. Gral. Paz 1499, 1650 San Martin, Buenos Aires, Argentina.*
[c] *Instituto de Nanosistemas. Universidad Nacional de San Martín (INS-UNSAM) Av. 25 de Mayo 1021, San Martín, Buenos Aires, Argentina.*

† Electronic Supplementary Information (ESI) available: [Experimental X-ray powder patterns, TG and DSC analysis, FTIR spectra and assignment of the excitation and emission transitions]. CCDC reference number 1477857-1477863 contains the supplementary crystallographic data for this paper. This data can be obtained free from the Cambridge Crystallographic Data Centre via: www.ccdc.cam.ac.uk/data_request/cif. See DOI: 10.1039/x0xx00000x

View Article Online
DOI: 10.1039/C6RA23516F

On the other hand, nanoindentation has been widely adopted to analyze the mechanical properties of thin films, single crystals and monoliths.[18] Thanks to pioneer works of Cheetham et al.,[19] nanoindentation analysis has been applied to demonstrate correlations between the internal arrangement of crystal packing and the anisotropic mechanical properties (density stability and elasticity) in MOF-type materials.

The present approach involves a complete and systematic study regarding the synthesis strategies, photophysical characterization, chemical sensing and for the first time, analysis of anisotropic mechanical properties on mixed ligand (naphtalenedisulfonate, phenanthroline) Ln-CPs.

Experimental Section

Synthesis

All reagents and solvents employed were commercially available and used as supplied with no further purification: 3-hydroxynaphthalene-2,7-disulfonic acid (95%, Sigma-Aldrich); 1,10-phenanthroline (99%, Sigma-Aldrich); $Ln(NO_3)_3.6H2O$ where Ln = Eu, Tb, Dy, Ho and Yb (99%, Sigma-Aldrich).

Several temperatures and reaction times were tested. The molar composition of the initial reaction mixture in $3\text{-}OHNDS^{3-}$: Ln^{3+}: 2Phen: $1474H_2O$ were set. The optimized synthesis procedure was the following:

$[Eu(3\text{-}OHNDS)(Phen)(H_2O)_2]\cdot 3H_2O$ (**Phase 1-Eu**) was obtained by the addition of 3-OHNDS (0.04 g, 0.116 mmol) and 1,10-phenanthroline (0.042 g, 0.232 mmol) to a solution of $Eu(NO_3)_3\cdot 6H_2O$ (0.05 g, 0.116 mmol) in 6 mL of distilled water under constant stirring at room temperature for 30 minutes. Finally, the reaction mixture was placed in a Teflon-lined stainless steel autoclave for reacting at 170˚C for 18 hours. After cooling at room temperature, the product mixture was filtered and washed with water and ethanol. Few small crystals were obtained and manually isolated for the product mixture.

Similar procedure was employed to obtain the compounds **$[Ln_2(3\text{-}OHNDS)_2(Phen)_2(H_2O)]\cdot 3H_2O$ (Phase 2-Ln)**, where Ln^{3+} = Tb, Dy, Ho, Er and Yb. **$[Ho_2(3\text{-}OHNDS)_2(Phen)_2(H_2O)]\cdot 3H_2O$** compound was obtained by the addition of 3-OHNDS (0.04 g, 0.115 mmol) and 1,10-phenanthroline (0.041 g, 0.23 mmol) to a solution of $Ho(NO_3)_3\cdot 6H_2O$ (0.05 g, 0.115 mmol) in 6 mL of distilled water under constant stirring at room temperature for 30 minutes. Finally, the reaction mixture was placed in a Teflon-lined stainless steel autoclave for reacting under hydrothermal conditions at 200˚C for 24 hours. After cooling to room temperature, the crystalline products (yield of 71.2 %) were filtered and washed with water and ethanol. Elemental analysis calculated (%) for **$[Ho_2(3\text{-}OHNDS)_2(Phen)_2(H_2O)]\cdot 3H_2O$:** C, 38.72; N,4.10; H, 2.51; S,9.4; found: C, 38.94 ; N,3.64; H, 2.83; S, 9.08.

Material Characterization

Single-Crystal structure determination. Single-crystal X-ray data was performed for **$[Eu(3\text{-}OHNDS)(Phen)(H_2O)_2]\cdot 3H_2O$** and **$[Ln_2(3\text{-}OHNDS)_2(Phen)_2(H_2O)]\cdot 3H_2O$** where Ln = Tb, Ho, Er and Yb were collected at room temperature (296 K) on a Bruker APEX-II CCD diffractometer, using MoKα radiation (0.71073 Å), monochromated by graphite. The cell determination and the final cell parameters were obtained on all reflections using the software Bruker SAINT included in APEX2 software suite.[20] Data integration and scaled was carried out using the software Bruker SAINT.[21] The compound $[Ho_2(C_7O_2H_5)_4(NO_3)_2]$ (Supp. Inf. S1) was collected on an Enraf-Nonius Kappa-CCD diffractometer using MoKα radiation (0.71073 Å), monochromated by graphite. The cell parameters were refined by Collect and Scalepack software and the final cell parameters were obtained for all reflections. Data reduction was carried out by Denzo-SMN and Scalepack software.[22]

The structures were solved by SHELXS-2013 software and then refined by SHELXL-2013,[23] included in WinGX[24] and Olex2.[25] Non-hydrogen atoms of the molecules were clearly resolved and their full-matrix least-square refinement was conducted using anisotropic thermal parameters. All hydrogen atoms were stereochemically positioned and refined by the riding model.[23] Hydrogen atoms of the water molecules were localized and fixed (with Uiso(H) = 1.5Ueq) on the density map. ORTEP diagrams were prepared with Diamond.[26] TOPOS,[27] Mercury[28] and Diamond[26] programs were used in the preparation of the artwork of the polyhedral and topological representations.

Powder X-ray diffraction (PXRD). Patterns were measured with a Rigaku Ultima IV diffractometer of 0.02˚ step size and 2 s/step exposure time. The measurements were used to prove the isostructurality of the series and check the purity of the microcrystalline products (Supp. Inf S7). Thermogravimetric analyses (TGA) and differential scanning calorimetry (DSC) were performed with Shimadzu TGA-50 and DSC-60 equipment at 25-900 ˚C and 25-300°C temperature range respectively (Supp. Inf. S2-S3). The measurements were performed under nitrogen (100 mL/min flow) atmosphere and 10 ˚C/min heating rate. A Fisons EA-1108 CHNS-O was employed for the elemental analysis. FTIR spectra were recorded from KBr pellets in the 4000-250 cm^{-1} range on a Bomem Michelson FT MB-102 (Supp. Inf. S4). Micrographs were obtained on FEI Quanta 200 microscope.

Photoluminescence (PL) measurements and sensing studies. The PL measurements were made on a Félix X32 PTI fluorometer setup equipped with a UXL-75Xe xenon short-arc lamp. For the excitation-emission spectra the samples were measured in ethanolic (≥ 99.8%, Biopack) suspensions (1 mg of compound in 3 mL of EtOH). Prior to the PL studies, the closed glass vials containing the samples were ultrasonicated at 80 KHz (in a Cleanson apparatus) for 60 minutes to obtain homogeneous suspensions. The slit widths for excitation and emission were 1.5 mm. Luminescence spectra were recorded at room temperature between 425-700 nm, all with identical operating conditions and with lamp on to ensure a valid comparison between the emission spectra. The data were collected at every nanometer with an integration time of 0.1 seconds for each step. Commission Internationale de l'Eclairage (CIE) (x,y) color coordinates were calculated using MATLAB® program. The sensing activity of **Tb** was investigated, monitoring the emission spectra at 541 nm and exciting the samples at 375

View Article Online
DOI: 10.1039/C6RA23516F

nm. The **Tb-nap**, **Tb-ani**, **Tb-tol** and **Tb-ant** suspensions were prepared introducing 1 mg of **Tb** powder into 3 mL (0.3 mg.mL^{-1}) of 0.01 M ethanolic solutions of toluene (Anedra, 99.8%), anthracene (Sigma-Aldrich, 97%), anisole (Merck, ≥99%), and naphthalene (Sigma-Aldrich, 99%). Previously the samples were ultrasonicated for 60 minutes to ensure an efficient substrate-sensor interaction.

Nanoindentation methodology on single crystals. Mechanical properties were measured by nanoindentation (NI) using a Nano Indenter Agilent G200 equipped with a Berkovich three-sided diamond pyramid tip with a rounding of 20 nm. A set of experiments was performed on the samples using a depth control method, indenting up to a maximum depth of 1200 nm in different locations. Oliver & Pharr model was applied to calculate Young's modulus and hardness (see Supp. Inf. S5).[29]

Results and discussion

Synthetic study

The choice of hydrothermal or solvothermal methodologies as the synthetic route of CPs and MOFs often involves several experiments to find optimal conditions (temperature, time, solvents, stoichiometry, pH, etc) in order to obtain pure crystalline materials.[30] The variables explored in this work include temperature, reaction time and solvothermal methodology, always under a fixed stoichiometry (see Exp. Section).

For the study of the hydrothermal reaction conditions, **Phase 2-Ln,** holmium derived was arbitrarily used for tests. **Phase 2**+ impurity mixture product (**Phase 2** >> impurity) was obtained as a result of low temperature test, where some peaks of the impurity coincides with **Phase 1** as shown in Supp. Inf. S6, a. These results indicate that both phases could be involved in a formation equilibrium where the **Phase 1** is formed and quickly transformed in the most stable **Phase 2**.

As it was observed in previous cases,[7, 31, 32] the electronic configuration and the lanthanide contraction impacted on the thermodynamic and kinetics of the reaction which enables to form different structural phases. For instance, two structural phases were obtained depending on the region of the lanthanide series. It was possible to find the **Phase 1** (La-Sm)[4] and **Phase 2** (Tb-Yb) in the "light rare-earth" region (LREE)[33] and "heavy rare-earth" region (HREE)[33] respectively.

Moreover, in order to compare the results employing solvothermal methodology under pre-defined synthesis conditions (200 °C, 24 h), different experiment were performed: i) Using methanol or ethanol, the **Phase 2** was obtained as a unique reaction product. ii) An unidentified phase and a mixture of decomposed products were obtained with acetonitrile and toluene respectively (Supp. Inf. S8). In fact, it was possible to isolate and characterize the compound **$[Ho_2(C_7O_2H_5)_4(Phen)(NO_3)_2]$** from the toluene reaction synthesis (Supp. Inf. S1). The formation of this compound indicates that it takes place in *situ* toluene oxidation under solvothermal conditions. Structural analysis for the isostructural Pr^{3+} compound was previously reported.[34]

Structural description of Ln-CPs. Details of the data collection as well as refinement and crystallographic data for the compounds are summarized in Table 1. The ORTEP diagrams for **$[Eu(3\text{-}OHNDS)(Phen)(H_2O)_2]\cdot 3H_2O$**, and **$[Tb_2(3\text{-}OHNDS)_2(Phen)_2(H_2O)]\cdot 3H_2O$** compounds are shown in Fig. 1.

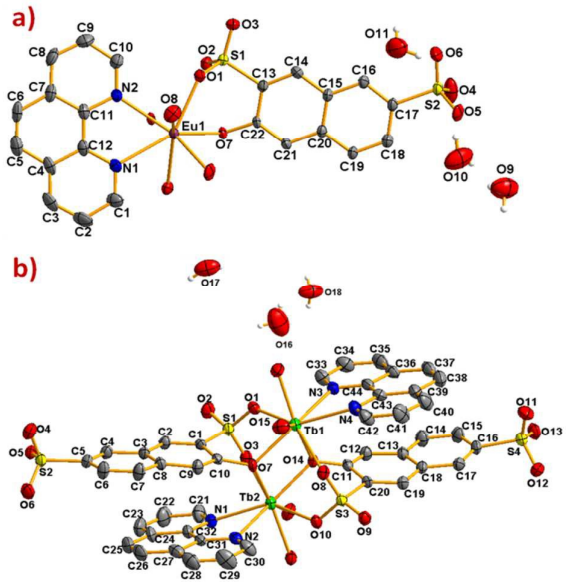

Fig. 1 ORTEP diagram showing 50% of probability ellipsoids **$[Eu(3\text{-}OHNDS)(Phen)(H_2O)_2]\cdot 3H_2O$** and **$[Tb_2(3\text{-}OHNDS)_2(Phen)_2(H_2O)]\cdot 3H_2O$** compounds. Hydrogen atoms were omitted for clarity.

The compound **$[Eu(3\text{-}OHNDS)(Phen)(H_2O)_2]\cdot 3H_2O$** was obtained within a mixture of reaction products. Small crystals were manually isolated and structurally characterized by single crystal X-ray diffraction. The compound crystallizes in the triclinic Pī space group (named here as **Phase 1**) belonging to a previously reported family of $[Ln(3\text{-}OHNDS)(Phen)(H_2O)_2]\cdot 3H_2O$ compounds,[4] (where Ln^{3+} = La, Pr, Nd and Sm). The asymmetric unit is formed by one crystallographically independent metal cation with the coordination of one 3-OHNDS ligand, one 1,10-phenanthroline and two water molecules.[4] The structure also presents three non-coordinated water molecules in the asymmetric unit. The particular coordination modes of the ligand give rise to ladder-shape chains as extended structure.

In **Phase 2-Ln, $[Ln_2(3\text{-}OHNDS)_2(Phen)_2(H_2O)]\cdot 3H_2O$** (Where, Ln^{3+} = Tb, Dy, Ho, Er and Yb), crystallizes in the monoclinic space group $P2_1/n$, as a pure phase. The asymmetric unit is formed by two crystallographically independent metallic centers with an 8-coordinate environment [Ln1 = Ln2 = square antiprism polyhedron (SAPR-8)][35] (Fig. 2). Furthermore, while defining the primary building units (PBU), the Ln1 is coordinated to: *(i)* Two nitrogen atoms of the 1,10-phenanthroline molecule, *(ii)* three oxygen atoms of the sulfonate group, *(iii)* two oxygen atoms of the phenyl group and *(iv)* one oxygen atom of the water molecule. Whereas, Ln2 coordination environment is formed by: *(i)* two nitrogen atoms of the 1,10-phenanthroline molecule, *(ii)* Four oxygen atoms of the sulfonate group and *(iii)* Two oxygen atoms of the

View Article Online
DOI: 10.1039/C6RA23516F

phenolate group. Dimeric shared edge secondary building units (SBUs) are formed by junction of the metallic centers via *syn-syn* $\mu\eta^2$ and $\mu\eta^2$ modes of two sulfonates and two phenolate groups, respectively. SBUs are linked along [101] crystallographic direction by the ligand through the sulfonate group giving rise to 1D ladder-shape coordination polymer. According to the classification proposed by Cheetham *et al.*,[36] these coordination polymers can be classified as *inorganic hybrid chains* I^1O^0; where I^1 means that the inorganic connectivity is 1D and O^0 implies that the organic one is zero-dimensional.

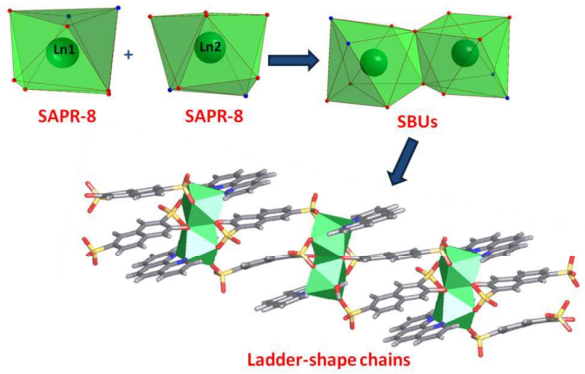

Fig. 2 Coordination polyhedron, SBU and chains formed by the **$[Ln_2(3\text{-}OHNDS)_2(Phen)_2(H_2O)]\cdot 3H_2O$** compounds.

The ladder-shape chains are joined together for the interstitial water molecules by strong hydrogen bonds. One water molecule links two chains along [100] direction with distances O18-H18B···O5 of 3.000(6) and O18-H18A···O11 of 2.814(7) Å respectively. Furthermore, Hydrogen (O17-H17B···O8 = 3.231(6), O16-H16B···O6 = 3.083(7) Å) and π-π stacking interactions between the 1,10-phenanthroline rings along [100] were noticed. An intercentroid distance 3.6002(1) Å was also observed, to complete the formation of 3D supramolecular crystal packing.

Structural comparison

Clear differences in the crystal packing of both phases are observed. The polymeric chains in **Phase 1** are formed along the [010] direction, while in **Phase 2** the same chains grow along [101] direction (Fig. 3).

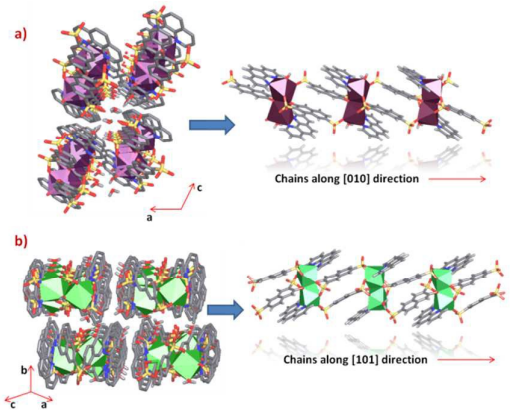

Fig. 3 Crystal packing and polymeric chains formation of a) **Phase 1** and b) **Phase 2** (some Hydrogen atoms from linkers were omited for clarity).

Through an analysis of the lanthanide coordination spheres, both phases are correlated by the loss of one coordination water molecule. This process provokes the coordination of one oxygen atom from the sulfonate group generating the re-orientation of the chains. Hence, resulting in the formation of two different crystal packing. Fig. 4, shows the formation of the thermodynamically stable *syn-syn* $\mu\eta^2$ mode in **Phase 2** accompanied with a ligand rotation of almost 180°.

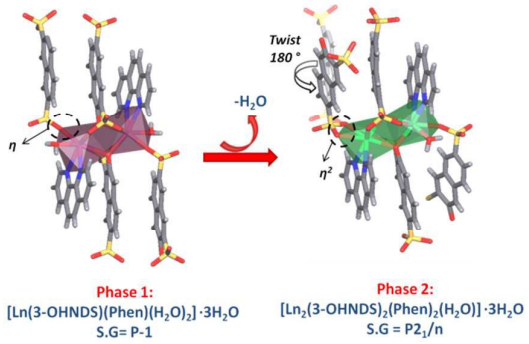

Fig. 4 Structural changes observed between **Phase 1** and **Phase 2**.

The differences in the crystal packing and the intermolecular interactions between both phases generate dissimilarities in the net topologies associated with such crystal structures. For this reason, TOPOS[16] program was employed to obtain the corresponding net simplifications. In both cases, the supramolecular packing is governed by multiple hydrogen bonds and weak hydrogen interactions. Considering the simplification of supramolecular network due to stronger hydrogen bonds, it is possible to get layer simplifications in both cases. Layers in **Phase 1** are formed by O18-H18A···O1 (2.935 Å) interactions which link the chains along [100] direction. 3-OHNDS ligand acts as ditopic connector joining two SBUs, while the dimeric SBU is linked to four connectors where both of them are hydrogen bonds (Fig. 5, a). This strong interaction gives rise to 2D layers in the (110) plane with **sql**/Shubnikov tetragonal plane topology and $[4^4.6^2]$ point symbol.[27]

View Article Online
DOI: 10.1039/C6RA23516F

In **Phase 2**, chains interact via O5···H18B-O18-H18A···O11 bonds along [100] direction giving rise to 2D supramolecular layers in the plane (101) with topology **3,5L52** and $[3.5^2][3^2.5^3.6^4.7]$ point symbol.[27] 3-OHNDS ligand acts as 3-connected node linking the 5-connected dimeric SBUs (Fig. 5, b).

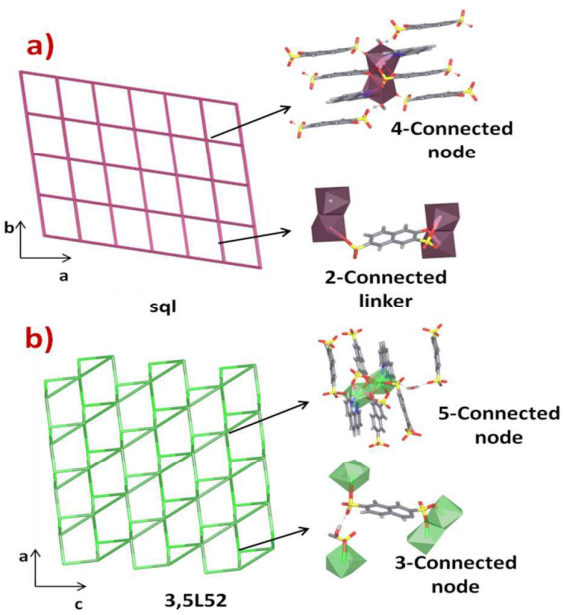

Fig. 5 Topological simplification of a) **Phase 1** and b) **Phase 2**.

Table 1. Crystallographic data and refinement parameters for $[Eu(3\text{-}OHNDS)(Phen)(H_2O)_2]\cdot 3H_2O$ and $[Ln_2(3\text{-}OHNDS)_2(Phen)_2(H_2O)]\cdot 3H_2O$ where Ln = Tb, Dy, Ho, Er and Yb compounds.

Compound	Eu	Tb	Ho	Er	Yb	Dy
Emp. Formula	$C_{22}H_{15}N_2O_8S_2Eu, 3(H_2O)$	$C_{44}H_{28}N_4O_{15}S_4Tb_2, 3(H_2O)$	$C_{44}H_{28}N_4O_{15}S_4Ho_2, 3(H_2O)$	$C_{44}H_{28}N_4O_{15}S_4Er_2, 3(H_2O)$	$C_{44}H_{28}N_4O_{15}S_4Yb_2, 3(H_2O)$	$C_{22}H_{15}N_2O_8S_2Dy, 3(H_2O)$
FW (g/mol)	704.48	1352.83	1364.85	1369.51	1381.07	1356.45
Temp. (K)	296	296	296	296	296	296
λ (Å)	0.71073	0.71073	0.71073	0.71073	0.71073	0.71073
Crystal system	Triclinic	Monoclinic	Monoclinic	Monoclinic	Monoclinic	Monoclinic
Space Group	$P\bar{1}$	$P2_1/n$	$P2_1/n$	$P2_1/n$	$P2_1/n$	$P2_1/n$
Unit cell						
a (Å)	9.2352(6)	14.2636(6)	14.2341(3)	14.2425(8)	14.2136(4)	14.2586(6)
b (Å)	11.8774(7)	17.0354(7)	17.0149(4)	17.0358(9)	17.0112(5)	17.0438(7)
c (Å)	12.6755(8)	18.9491(7)	18.8852(4)	18.8857(10)	18.8325(5)	18.9287(7)
α (˚)	106.681(3)	90	90	90	90	90
β (˚)	110.149(3)	99.088(2)	98.991(1)	99.030(2)	99.014(1)	99.071(1)
γ (˚)	99.171(3)	90	90	90	90	90
Volume ($Å^3$)	1197.7(1)	4546.6(3)	4517.6(2)	4525.5(4)	4497.3(2)	4542.5(3)
Z	2	4	4	4	4	4
ρ calcd (mg/m^3)	1.863	1.976	2.007	2.010	2.040	1.984
Abs.Coeff (mm^{-1})	1.935	3.354	3.747	3.953	4.404	3.532
F(000)	691	2656	2672	2680	2696	2653
θ range (˚)	1.8 to 26.5	1.6 to 26.5	1.6 to 26.4	1.6 to 26.4	1.6 to 26.4	1.6 to 26.4
Reflections collected / Unique [R(int)]	21024/4955 [0.059]	140387/9363 [0.104]	32602/9231 [0.043]	129298/9276 [0.051]	60860/9216 [0.060]	89917/9287 [0.090]
Completeness (%)	99.8	99.4	99.5	99.9	99.8	99.8
Data / restraints / parameters	4955/0/341	9363/0/647	9231/0/647	9276/0/647	9216/0/647	9287/0/655
Gof on F^2	1.05	1.12	1.02	1.09	1.03	1.03
R1 [I>2σ(I)]	0.0354	0.0365	0.0305	0.0242	0.0276	0.0361
wR2[I>2σ(I)]	0.0894	0.0927	0.0658	0.0588	0.0576	0.0870

View Article Online
DOI: 10.1039/C6RA23516F

Journal Name

ARTICLE

Nanomechanical properties

To elucidate structural-mechanical properties and relationships underlying the 3D framework, NI experiments were performed on selected single crystals of **Phase 2-Yb** as representative model. **Phase 2-Yb** was chosen as being the larger crystal of all the series, Fig. 6. The crystal faces were identified via single-crystal X-ray diffraction (see Fig. 6, a). The crystal indexing was carried out using Mercury program (Fig. 6, b).[28] The orientations (010), (1 0-1) and (001) of crystal faces were indented at a maximum penetration depth of 1200 nm (Fig. 6, c). With the purpose of avoiding ambiguities, NI experiments on the acrylic substrate were made without crystals (see *P-h* curves in Fig. 7), with *H* and *E* values of 0.18±0.01 and 4.5±0.2 GPa.

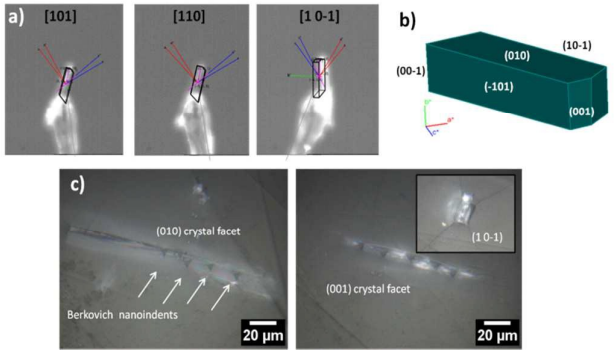

Fig. 6 a) Experimental procedure to determine the different facets of a **Phase 2-Yb** single crystal. b) Crystal model and c) Micrograph of single crystals of **Phase 2-Yb** in different exposed *hkl*-oriented facets. In the same figures the *Berkovich* indents made to a maximum depth of 1200 nm are indicated.

Load-displacement (*P-h*) curves obtained on the natural facets of single crystals of **Phase 2-Yb** are shown in Fig. 8. The average values of hardness (*H*) and Young's modulus (E), extracted from *P-h* curves of the three main faces are: *(i)* 0.32±0.03 and 7.8±0.5 GPa, *(ii)* 0.22±0.02 and 5.6±0.3 GPa and *(iii)* 0.05±0.02 and 3.2±0.6 GPa, assigned to (010), (001) and (10-1) faces respectively. This assignation was based on structural features.

Phase 2-Yb NI analysis shows high modulus values in (010) and (001) faces. The indentation along [101] confers the highest stiffness in the crystal structure. It is due to the indenter axis, which in this case aligns parallel to the chains growth direction. However, along [110] direction (stacking chains direction, Fig. 8, b), the modulus decreases by 28.2% with respect to the previous value.

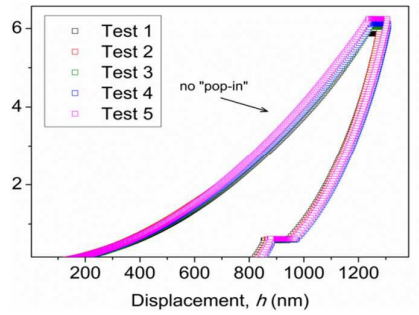

Fig. 7 *P-h* profiles of the acrylic without crystals.

Moreover, a decrease in *H* and *E* values shall be expected when the indenter is perpendicular to (101) plane. It could be explained in terms of the weak interactions exhibited in that plane, (hydrogen bonds and π-π interactions, Fig. 8, c). The same behavior was previously reported by Tan, *et al.*, where $[Cu_3(H_2O)_2(O_3PCH_2CO_2)_2]$ compound is formed by layers parallels to (010) plane. The authors reported the highest modulus values in the direction of the layer formation [011] and [110] (61.2±2.2 and 55.2±1.1 GPa, respectively) and low value in the stacking layer direction (34.5±0.9 GPa).[37]

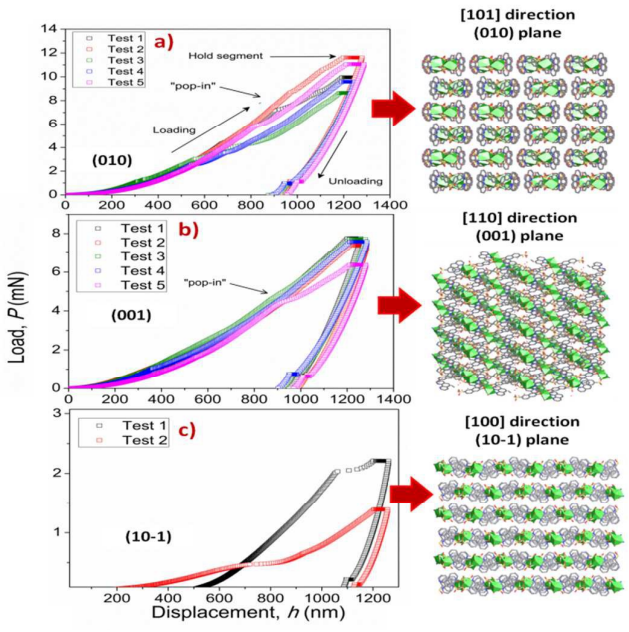

Fig. 8 *P-h* profiles of the **Phase 2-Yb** crystals in comparison with the crystal packing along the main crystallographic orientations.

View Article Online
DOI: 10.1039/C6RA23516F

It is important to remark the presence of "pop-in" or *displacement events* detected on all crystal faces (see Fig. 8), being an intrinsic characteristic of the material. This phenomenon could be explained for the breakages of weaker bonds and chain deformation (see crystallographic section), being more prominent in (010) plane. Same displacements have been described in low dimensional MOFs such as $[Cu_3(H_2O)_2(O_3PCH_2CO_2)_2]$[37] and [Mn(2,2-dimethylsuccinate)].[38] Tan *et al*,.[19] associated the presence of "pop-in" events to *plastic deformations* in the (001) plane of [Ce(oxalate)(formiate)]. It is notorious the absence of "pop-in" steps when NI experiments were carried out on acrylic without **Phase 2-Yb** crystals (Fig. 7). To put these results in context, it is necessary to make comparisons with related compounds. As far as we know, this work is the first to report the mechanical properties of coordination polymers based on sulfonate linker. According to the *E* vs *H* map (Fig. 9), it was possible to locate **Phase 2-Yb** between organic polymers and ceramics. For comparison, *E* values found for **Phase 2-Yb** are close to that reported for ZIFs (zeolitic imidazole frameworks) materials (3-9 GPa).[39]

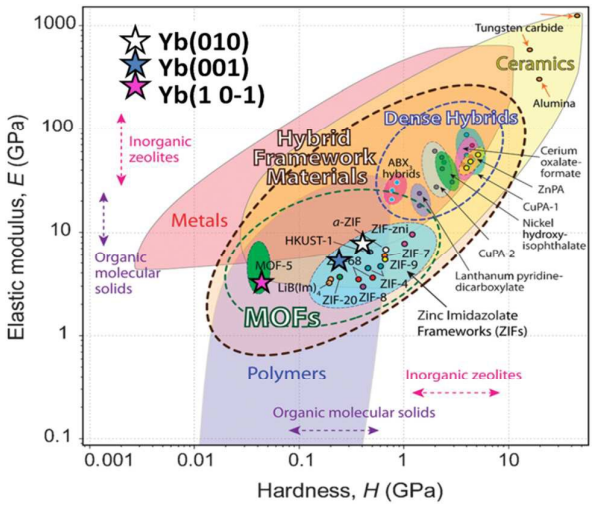

Fig. 9 Young's modulus *vs* hardness for different materials (from Tan, *et al*.,).[29] The *E* and *H* values of different crystal facets of **Phase 2-Yb** are included (stars) in comparison with other MOF-type materials.

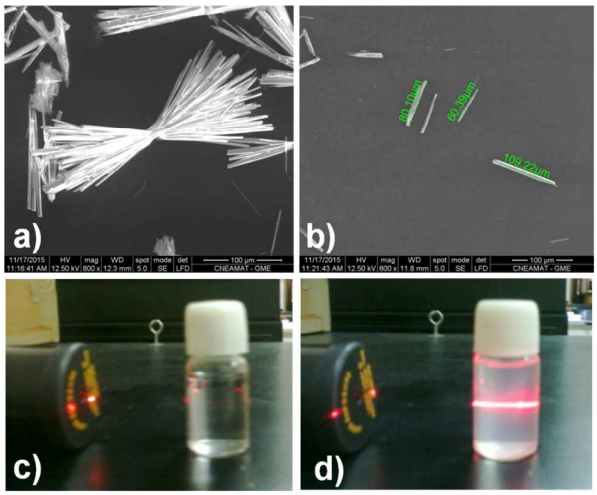

Fig. 10 a) SEM micrographs of "double-head broom-like" crystals, and b) ultrasonicated needle-shape crystals of **Yb**. Demonstration of the *Tyndall effect* in colloidal suspensions containing ultrasonicated **Yb** crystals. c) The path of the red laser beam is invisible in ethanol (ignoring reflections by the glass surfaces). d) The laser beam is clearly visible through the colloidal ethanolic suspension of 0.3 mg.mL^{-1} of **Yb** crystals.

Luminescence properties

In order to make the photophysical characterization, a pre-treatment liquid ultrasonication (LU) was performed (from now on named for its metal component to simplify the notation, e.g. **Phase 2-Yb** = **Yb**). LU has been employed as a "top-down" route to exfoliate low dimensional MOFs materials.[38, 40] As can be seen in Fig. 10 a, the as-synthesized Ln-CPs compounds (bulk phase) are obtained with a high degree of crystal condensation, forming "double-head broom-like" structures. By LU, the big structures are separated in "needle" shaped crystals with lengths between 60-100 µm and widths of ~8 µm (Fig. 10, b). We have recently demonstrated the impact of the crystal condensation on the PL properties of 2D Eu-MOFs, showing that miniaturization-exfoliation procedures decreased non-radiative pathways.[41] Fig. 10 d, shows the system containing the ultrasonicated **Yb** crystals in ethanol (density 0.3 mg.mL^{-1}), illuminated with a red laser. As a consequence, the ethanolic suspension containing the needle-shaped crystals shows the characteristic *Tyndall effect* associated with colloidal systems. The nature of the ultrasonicated samples was studied by PXRD and FTIR techniques (see Supp. Inf. S10, S11 and S12). The PXRD pattern of ultrasonicated crystals showed preferred orientation of the (020) crystallographic plane (Supp. Inf. S11). This is expected due LU takes places through that direction in which hydrogen bonds ensure crystalline packing. According with the vibrational study (Supp. Inf. 11), the band located at 1668 cm^{-1} associated with the bending mode of water molecules, is affected by LU. Meanwhile the bands at 2854 and 2925 cm^{-1} related to νC-H aromatic modes are more intense after exfoliation, indicating that the LU occurs in the mentioned direction. These results confirmed the presence of a unique phase consistent with the bulk one.

Due to the intense increment of investigations of luminescent MOFs,[42, 43] it was possible to identify basic steps in order to explore the PL properties. These studies include the collection of the PL spectra, quantum yields (QYs) and lifetime values (τ_{obs}). In this sense, the quantification of the emitting light color is relevant to elaborate optical devices as chemical[17] and physical sensors.[44, 45] In this work, the room temperature PL properties for **Eu**, **Tb**, **Dy** ("early" Ln^{3+}), **Ho**, **Er** and **Yb** ("late" Ln^{3+}) are reported and compared to analogous Ln^{3+}/3-OHNDS coordination polymers (Ln = La, Pr, Nd, Sm).[4]

After monitoring the excitations at specific wavelengths [excitation spectrum of **Eu** monitoring at 611 nm ($^5D_0 \rightarrow {}^7F_2$), **Tb** at 545 nm ($^5D_4 \rightarrow {}^7F_5$), **Dy** at 573 nm ($^7F_{9/2} \rightarrow {}^6H_{13/2}$), and **Ho**, **Er** and **Yb** at 430 nm], a dominance of aromatic π→π*/n→n* transitions bands (300-400 nm range) was observed. [46] (see

View Article Online
DOI: 10.1039/C6RA23516F

Fig. 11). Some compounds exhibited both ligands and 4f transitions (**Eu**, **Tb**, **Dy**). So, the selected excitation wavelengths (λ_{exc}) were 391 (25575 cm^{-1}), 375 (26667 cm^{-1}), 385 (25974 cm^{-1}), 374 (26738 cm^{-1}), 345 (28986 cm^{-1}) and 338 nm (29586 cm^{-1}) for **Eu**, **Tb**, **Dy**, **Ho**, **Er** and **Yb** respectively. This fact indicates a rather *antenna effect,* as it was seen in analogous Ln-CPs .[4]

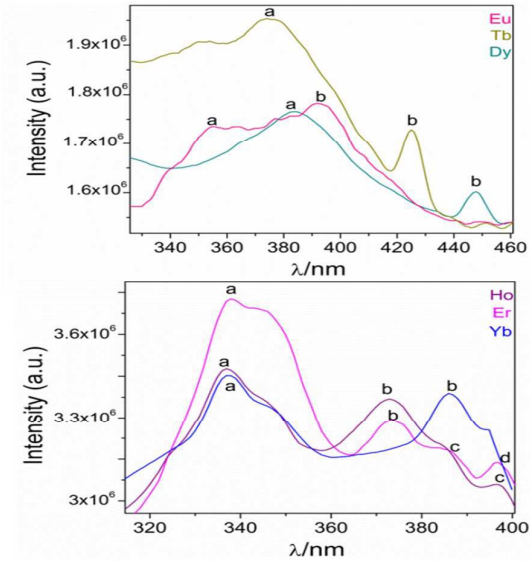

Fig. 11 Excitation spectra of Ln-CPs. The corresponding assignations of labelled transitions can be found in Supp. Inf. S9.

From excitation spectrum for **Eu** (Fig. 11) two maximum peaks related to ligand (label a, 362 nm) and $^5L_6 \rightarrow {}^7F_0$ Eu^{3+} (label b, 391 nm) transitions were located. It is worth to mention that $^5L_6 \rightarrow {}^7F_0$ transition is the highest peak in excitation spectrum of carboxylates Eu-MOFs.[47, 48] In order to evaluate possible transfer phenomena, two experiments were carried out employing two different excitation wavelengths as shown in Fig. 12 a. The resulting emission spectra show strong *ligand centered luminescence* (LCL) accompanied by a weak signal corresponding to $^5D_0 \rightarrow {}^7F_2$ transition (label as f in **Eu-362** and **Eu-391**). This 4f transition is more intense when the sample is excited at 362 nm (27624 cm^{-1}), evidencing possible energy migrations not only from ligand, but also from $^5D_0$ europium emissive level (19020 cm^{-1}). These facts indicate a more efficient emission process when an excitation wavelength is selected close to the ligand absorption edge. The direct excitation into 4f levels ($^7F_6 \rightarrow {}^5H_7$) in **Tb** exhibit an intense $^5D_4 \rightarrow {}^7F_J$ (J = 5, 4, 3, 2 and 0) transitions (**Tb-425**), (labelled as e-h see Supp. Inf. S9). These are the most intense bands belonging to the organic molecules (labelled as c-d). The excitation at 375 nm (spectrum **Tb-375**) led to emissions dominated by ligand bands (labelled as c-f) accompanied by the Tb^{3+} ion's shell (labelled as g-j). In **Tb-375** and **Tb-425** spectra, the most intense 4f peak was the $^5D_4 \rightarrow {}^7F_5$ transition. In the literature, this signal has been used to study the chemical sensor performance in many Tb-MOFs.[49, 50] The optical behavior of **Dy** was also evaluated, exciting the sample at two different wavelengths. At λ_{exc} = 385 nm (25974 cm^{-1}) the emission is dominated mainly by ligand bands with a poor contribution of 4f Dy^{3+} transitions (spectrum **Dy-385**); meanwhile at λ_{exc} = 446 nm (22422 cm^{-1}) bands of aromatic linkers and some 4f transitions were identified. In Dy-MOFs,[51, 52] the most intense transition is $^7F_{9/2} \rightarrow {}^6H_{13/2}$ (see spectrum of **Dy-446**, Fig. 12, c). On the other hand, **Ho**, **Er** and **Yb** compounds showed LCL characterized by $\pi^* \rightarrow \pi$/ $n^* \rightarrow n$ transitions in the visible range (see Fig. 12, d), without 4f transitions.

The behavior of strong quenching of Eu^{3+} emission ions and the low dominance of Tb^{3+} transitions could be explained by *multiphonon relaxation mechanism*, previously reported for Eu and Tb-MOFs.[53] The presence of two coordination (one in **Tb** and **Dy**) and three hydration water molecules per metal center in **Eu**, contribute to non-radiative pathways. Secondly, the *concentration quenching of luminescence* (condensation of emitting centers) is attributed for 4f emission attenuation. For instance, the proximities between the Ln-polyhedra (3.759 and 3.678 Å, for **Tb** and **Yb** respectively) in Ln/3-OHNDS are shorter compared to the Ln-2,3-dimethylsuccinate (4.3001(1) Å)[54], whose decrease in 4f intensity transitions was explained by this mechanism.

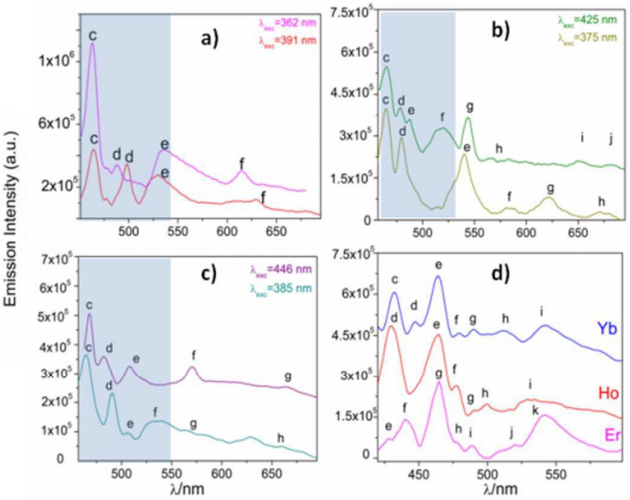

Fig. 12 a) Emission spectra of **Eu** (a), **Tb** (b), **Dy** (c) and **Ho**, **Er** and **Yb** (d). The corresponding labels are shown in Supp. Inf. S9. The marked blue zone denotes LCL.

Quantification of luminescence: analysis of CIE x,y chromaticities

The quantification of the color (QC) emission in luminescent materials enables an accurate comparison between different materials, concerning their light-emitting performance. In this sense, the color coordinates are usually calculated employing the CIE (Commision International de L'Éclairage) system, proposed in 1931.[55] The QC is relevant for lanthanide device fabrication for many purposes.[56, 57] In this context, the color emission of **Eu, Tb**, **Dy, Ho, Er** and **Yb** were quantified in terms of *x, y* color coordinates and compared to analogous phases.

View Article Online
DOI: 10.1039/C6RA23516F

Eu, Tb and **Dy** compounds have different light-emitting behavior (see Fig. 13 a, b and c). The predominance of blue color in this new set of compounds is explained by the influence of 3-OHNDS ligand. Intrinsically, the 3-OHNDS ligand emits blue colour[4] (*x, y* = 0.14, 0.1). Similar features could be found in analogous phases,[4] where majority of the samples presented *x, y* coordinates belonging to blue zone of the CIE diagram, except **[Sm(3-OHNDS)(H_2O)$_2$]** and **[Sm(3-OHNDS)(Phen)(H_2O)].3H_2O**, which emitted pink and white light. Besides, the character of white-light emission from **Dy-446** is remarkable, exhibiting *x, y* coordinates 0.32, 0.37 close to dysprosium based-white emitters (0.33, 0.33).[58, 59] This fact is a highlighted feature of solid-state lighting, full color display and backlights[60-62] in front of other co-doped materials, because it is not necessary to add any other lanthanide into the structure to produce white light. As it was described before, **Ho, Er** and **Yb** showed basically LCL, exhibiting *x, y* coordinates into the blue zone of CIE diagram (see Fig. 13). The Table in the Supp. Inf. S13 summarizes the QC data of so far reported coordination polymers based on lanthanides and 3-OHNDS.

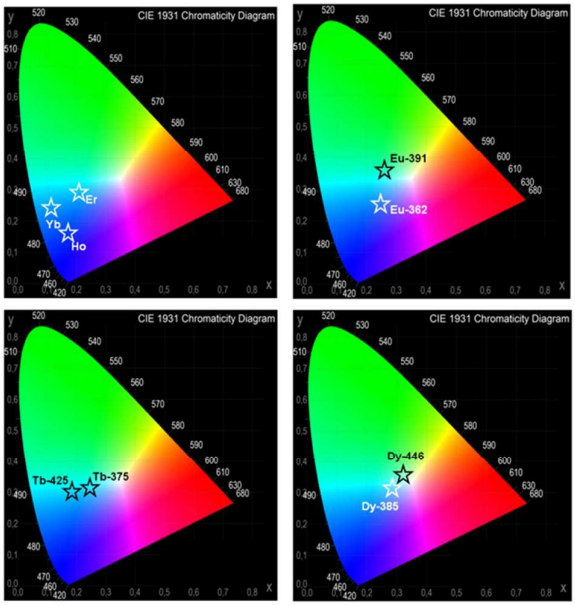

Fig. 13 CIE diagrams for the studied systems. Corresponding *x,y* coordinates are displayed in Supp. Inf. S13

Sensing studies

There are many examples reporting sensing of vapor, liquid and substances in solution by fluorescence, quenching and enhancement processes. Lanthanide and metal transition MOFs have been employed as platforms to sense organic solvents,[63] VOCs (volatile organic compounds),[64] water[65] and ions.[50] Besides this, the use of these compounds in the detection of hazardous materials such as explosives[66] is a significant issue regarding security and safety measures. It is worth to mention that the study of CPs or MOFs formed from naphthalene-linkers with applications as sensor platforms is really scarce. One relevant example is the work of Takashima *et. al.*[67] In this report they obtained a porous [Zn(BDC)2(dpNDI)] MOF(BDC = 1,4-benzenedicarboxylate; dpNDI = N,N'-di(4-pyridyl)-1,4,5,8-naphthalenediimide), with PL properties depending on the guest aromatic molecules.

Generally, authors quantify quenching effect by calculating the *Quenching Efficiency* (QE) defined as $(I_0\text{-}I)/I_0$ x 100%, where I_o and *I* represent the intensity values before and after exposure, respectively.

To study the sensor capability of this new set of CPs, **Tb** was selected as sensor model. According to the photophysical characterization, **Tb** showed dual luminescence centered at 464 nm (LCL) and at 541 nm (LnCL and $^5D_4 \rightarrow {}^7F_5$ transition). Two VOCs (toluene and anisole) and two PAHs (polycyclic aromatic hydrocarbons) (anthracene and naphthalene) were chosen to study the sensor performance of **Tb** towards the intensity emission as signal transduction. Fluorescence measurements were carried out in a 1 cm quartz cuvette, containing some milligrams of **Tb** sample suspended in ethanol solutions of aromatics (for more details see experimental section). Figures 14 a and b show the emission spectra of **Tb-nap**, **Tb-tol**, **Tb-ani** and **Tb-ant** (λ_{exc} = 375 nm) in the LCL and LnCL region.

Fig. 14-a, shows the LCL of **Tb** is incremented in anisole (23.6%) and anthracene but quenched in naphthalene (QE = 51.6%). The LCL zone of **Tb-ant** is not complete because its signal is high enough that it saturated the fluorometer detector. In Fig. 14-a, only one portion of Tb-ant signal is shown. Furthermore, 4f quenching effect is seen in presence of anisole and anthracene (QE = 37.4% and 26.1% respectively). However, it is enhanced in 18.4% when **Tb** interacted with naphthalene (Fig. 14-b). The spectrum of **Tb-tol,** did not show any drastic changes in intensity. As it can be observed in Fig. 14-b, the 4f signal of **Tb-ant** was quenched and suffered a blue shift (Δλ=14 nm). To the extent of our knowledge, this is the first example of *hypsochromic* shift in a 4f-4f emission transition in Tb-MOFs materials.

View Article Online
DOI: 10.1039/C6RA23516F

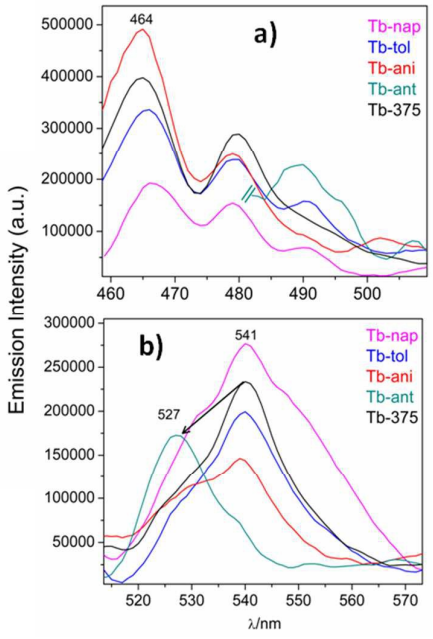

Fig. 14 a) Emission spectra of **Tb-nap, Tb-tol, Tb-ani** and **Tb-ant** zoomed into the LCL and b) $^5D_4 \rightarrow {}^7F_5$ emission zone.

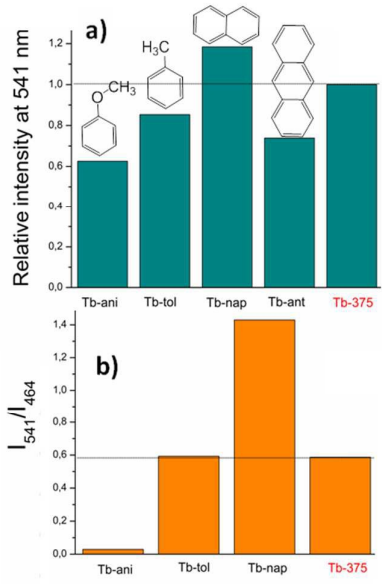

Fig. 15 a) Variations of the relative intensity centered at 541 nm and b) intensities ratio (I_{541}/I_{464}).

The CP-substrate interactions directly impacted on the intensities ratio I_{541}/I_{464} (see Fig. 14, e) in a major degree, when naphthalene molecules interacted with the emissive Tb^{3+} centers. This differential optical activity could be explained in terms of the *photoelectron transfer* (PET) process between the aromatics molecules with the different emissive sites. Finally, a QC was carried out (Fig. 14, e). This analysis reflected differences in the colorimetric response of Tb under different chemical environments around the emissive material: green luminescence in naphthalene (x,y=0.26, 0.5), blue in anisole (x,y=0.22, 0.26) and blue-green in toluene solution (x,y=0.26, 0.31). It is also observed that the sensing did not affect the vibrational behavior of **Tb** (see Supp. Inf. S14).

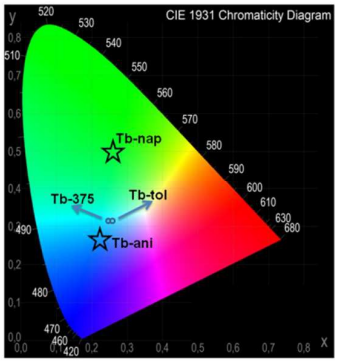

Fig. 16 Chromaticity diagram of **Tb-nap**, **Tb-tol**, **Tb-ani** and **Tb-ant** in comparison with **Tb-375**.

Conclusions

As a product of hydrothermal synthesis of the series of lanthanide metals with the 3-OHNDS and 1,10-phenanthroline ligands, two different crystalline phases were obtained and fully characterized. A general behavior was observed with the formation of the different phases, where the "LREE" metals (La-Eu) gave rise to the formation of the **Phase 1**, while **Phase 2** is obtained with the "HREE" lanthanides (Tb-Yb). As it was demonstrated, Eu^{3+} can be described as the inflection point which divides the two phases. Structural differences are caused by the loss of one coordinated water molecule, triggering the rearrangement of the packing and the symmetry changes. The 2D supramolecular network was topologically simplified as **sql** and **3,5L52** for the **Phase 1** and **2** respectively. Moreover, nanoindentations on single-crystals showed anisotropic elastic modulus and hardness. This is the first example of such type of characterizations in sulfonate-coordination polymers. The degree of anisotropy along the crystallographic faces could be directly correlated to the crystalline structure. It was evidenced that the presence of strong covalent bonding interactions (Ln-O-Ln) accompanied by weak interactions within the same framework which could lead to highly directional mechanical responses.

A comprehensive characterization of the PL properties of the reported phases was performed. The optical performance is mainly dominated by LCL accompanied by 4f-transitions. The quenching of the 4f emissions could be explained by two non-radiative mechanisms: *multiphonon relaxation*, and *concentration quenching of luminescence*. At this point, it is important to mention that an almost white-light **Dy** emission was obtained. Also, the activity of **Tb** compound as chemical sensor was evaluated. The intensities ratio parameter was used as a tool for distinguishing the presence of different

View Article Online
DOI: 10.1039/C6RA23516F

aromatic compounds. Moreover, a hypsochromic shift transition of a Tb-CP has been observed.

With all these results in mind, it was possible to establish structural-mechanical-optical relationships. The combination of sensor activity along with elastic and hardness anisotropy makes these compounds multifunctional materials with emerging applications.

Notes and references

Corresponding Author

* To whom correspondence should be addressed to e-mail: ridvries@ifsc.usp.br Fax: +55 (16) 3373-9758 or gegomez@unsl.edu.ar.

Author Contributions

The manuscript was written through contributions of all authors. All authors have given approval to the final version of the manuscript.

Acknowledgments

R. D. acknowledges Coordenação de Aperfeiçoamento de Pessoal de Nivel Superior for the CAPES/PNPD scholarship from the Brazilian Ministry of Education, to M. Soto-Monsalve and R. de Almeida Santos for measurements and FAPESP (2009/54011-8) for providing Apex-II equipment. J.E. is grateful to CNPq for the research fellowships. G. E. G. acknowledges CONICET (Consejo Nacional de Investigaciones Científicas y Técnicas) for the postdoctoral fellowship and INTEQUI-UNSL for the TGA analysis. D.F.L. acknowledges CONICET doctoral fellowship. G.J.A.A.S.I. and M.C.F. are members of CIC-CONICET.

References

1. O. M. Yaghi, M. O'Keeffe, N. W. Ockwig, H. K. Chae, M. Eddaoudi and J. Kim, *Nature*, 2003, **423**, 705-714.
2. C. B. Aakeroy, N. R. Champness and C. Janiak, *CrystEngComm*, 2010, **12**, 22-43.
3. R. F. D'Vries, V. A. de la Peña-O'Shea, Á. Benito Hernández, N. Snejko, E. Gutiérrez-Puebla and M. A. Monge, *Cryst. Growth Des.*, 2014, **14**, 5227-5233.
4. R. F. D'Vries, G. E. Gomez, J. H. Hodak, G. J. A. A. Soler-Illia and J. Ellena, *Dalton Trans.*, 2016, **45**, 646-656.
5. A. E. Platero-Prats, M. Iglesias, N. Snejko, A. n. Monge and E. Gutiérrez-Puebla, *Cryst. Growth Des.*, 2011, **11**, 1750-1758.
6. F. Gándara, E. G. r. Puebla, M. Iglesias, D. M. Proserpio, N. Snejko and M. A. n. Monge, *Chem. Mater.*, 2009, **21**, 655-661.
7. R. F. D'Vries, M. Iglesias, N. Snejko, E. Gutiérrez-Puebla and M. A. Monge, *Inorg. Chem.*, 2012, **51**, 11349-11355.
8. F. Gándara, E. Gutiérrez-Puebla, M. Iglesias, N. Snejko and M. A. n. Monge, *Cryst. Growth Des.*, 2009, **10**, 128-134.
9. J. Perles, M. Iglesias, M.-Á. Martín-Luengo, M. Á. Monge, C. Ruiz-Valero and N. Snejko, *Chem. Mater.*, 2005, **17**, 5837-5842.
10. K. Müller-Buschbaum, F. Beuerle and C. Feldmann, *Micropor. Mesopor. Mater.*, 2015, **216**, 171-199.
11. R. F. D'Vries, S. Alvarez-Garcia, N. Snejko, L. E. Bausa, E. Gutierrez-Puebla, A. de Andres and M. A. Monge, *J. Mater. Chem. C*, 2013, **1**, 6316-6324.
12. F. Gandara, N. Snejko, A. d. Andres, J. R. Fernandez, J. C. Gomez-Sal, E. Gutierrez-Puebla and A. Monge, *RSC Adv.*, 2012, **2**, 949-955.
13. S. Horike, D. Umeyama and S. Kitagawa, *Acc. Chem. Res.*, 2013, **46**, 2376-2384.
14. R. F. D'Vries, I. Camps and J. Ellena, *Cryst. Growth Des.*, 2015, **15**, 3015-3023.
15. R. F. D'Vries, V. A. de la Peña-O'Shea, N. Snejko, M. Iglesias, E. Gutiérrez-Puebla and M. A. Monge, *J. Am. Chem. Soc.*, 2013, **135**, 5782-5792.
16. J. C. G. Bünzli and C. Piguet, *Chem. Soc. Rev.*, 2005, **34**, 1048-1077.
17. Z. Hu, B. J. Deibert and J. Li, *Chem. Soc. Rev.*, 2014, **43**, 5815-5840.
18. A. Gouldstone, N. Chollacoop, M. Dao, J. Li, A. M. Minor and Y.-L. Shen, *Acta Mater.*, 2007, **55**, 4015-4039.
19. J. C. Tan, J. D. Furman and A. K. Cheetham, *J. Am. Chem. Soc.*, 2009, **131**, 14252-14254.
20. I. Bruker-AXS, *APEX2 Software Suite*, 2; Madison, WI., 2006.
21. I. Bruker-Siemens, *SAINT*, V 6.28A; Madison, WI., 1997.
22. Z. Otwinowski and W. Minor, *Methods in Enzymology*, Academic Press, New York, 1997.
23. G. Sheldrick, *Acta Crystallogr. Sect. A*, 2008, **64**, 112-122.
24. L. Farrugia, *J. Appl. Crystallogr.*, 2012, **45**, 849-854.
25. O. V. Dolomanov, L. J. Bourhis, R. J. Gildea, J. A. K. Howard and H. Puschmann, *J. Appl. Crystallogr.*, 2009, **42**, 339-341.
26. H. P. K. Brandenburg, *DIAMOND- Crystal and Molecular Structure Visualization*, Crystal Impact: Kreuzherrenstr. 102, 53227 Bonn, Germany, 2006.
27. V. A. Blatov, A. P. Shevchenko and D. M. Proserpio, *Cryst. Growth Des.*, 2014, **14**, 3576-3586.
28. C. F. Macrae, I. J. Bruno, J. A. Chisholm, P. R. Edgington, P. McCabe, E. Pidcock, L. Rodriguez-Monge, R. Taylor, J. Van De Streek and P. A. Wood, *J. Appl. Crystallogr.*, 2008, **41**, 466-470.
29. J. C. Tan and A. K. Cheetham, *Chem. Soc. Rev.*, 2011, **40**, 1059-1080.
30. N. Stock and S. Biswas, *Chem. Rev.*, 2012, **112**, 933-969.

View Article Online
DOI: 10.1039/C6RA23516F

31. R. F. D'Vries, V. A. de la Peña-O'Shea, N. Snejko, M. Iglesias, E. Gutiérrez-Puebla and M. Á. Monge, *Cryst. Growth Des.*, 2012, **12**, 5535-5545.
32. R. F. D'Vries, N. Snejko, M. Iglesias, E. Gutiérrez-Puebla and M. A. Monge, *Cryst. Growth Des.*, 2014, **14**, 2516-2521.
33. P. Henderson, in *Developments in Geochemistry*, ed. P. Henderson, Elsevier, 1984, vol. Volume 2, pp. 1-32.
34. Z. L.-G. XIAN Chun-Ying, YU Qing-Sen, *Chem. J. Chinese U.*, 1999, **20**, 1504-1508.
35. N. G. Connelly, ; Damhus, T.;Hartshorn, R.M.; Hutton, A.T., *Nomenclature of Inorganic Chemistry - IUPAC Recommendations 2005*, RSC Publishing, Cambridge, UK., 2005.
36. A. K. Cheetham, C. N. R. Rao and R. K. Feller, *Chem. Commun.*, 2006, 4780-4795.
37. J. C. Tan, C. A. Merrill, J. B. Orton and A. K. Cheetham, *Acta Mater.*, 2009, **57**, 3481-3496.
38. J.-C. Tan, P. J. Saines, E. G. Bithell and A. K. Cheetham, *ACS Nano*, 2012, **6**, 615-621.
39. J. C. Tan, T. D. Bennett and A. K. Cheetham, *Proceedings of the National Academy of Sciences*, 2010, **107**, 9938-9943.
40. Y. Peng, Y. Li, Y. Ban, H. Jin, W. Jiao, X. Liu and W. Yang, *Science*, 2014, **346**, 1356-1359.
41. G. E. Gomez, M. C. Bernini, E. V. Brusau, G. E. Narda, D. Vega, A. M. Kaczmarek, R. Van Deun and M. Nazzarro, *Dalton Trans.*, 2015, **44**, 3417-3429.
42. M. D. Allendorf, C. A. Bauer, R. K. Bhakta and R. J. T. Houk, *Chem. Soc. Rev.*, 2009, **38**, 1330-1352.
43. Y. Cui, Y. Yue, G. Qian and B. Chen, *Chem. Rev.*, 2011, **112**, 1126-1162.
44. E. C. Spencer, J. Zhao, N. L. Ross, M. B. Andrews, R. G. Surbella and C. L. Cahill, *J. Solid State Chem.*, 2013, **202**, 99-104.
45. Y. Cui, F. Zhu, B. Chen and G. Qian, *Chem. Commun.*, 2015, **51**, 7420-7431.
46. G. Accorsi, A. Listorti, K. Yoosaf and N. Armaroli, *Chem. Soc. Rev.*, 2009, **38**, 1690-1700.
47. G. E. Gomez, A. M. Kaczmarek, R. Van Deun, E. V. Brusau, G. E. Narda, D. Vega, M. Iglesias, E. Gutierrez-Puebla and M. Á. Monge, *Eur. J. Inorg. Chem.*, 2016, **2016**, 1577-1588.
48. S. R. Russell, C. Gosset, X. Agache, C. Volkringer, N. Henry, R. Decadt, R. Van Deun, M. Visseaux and T. Loiseau, *CrystEngComm*, 2016.
49. K. L. Wong, G. L. Law, Y. Y. Yang and W. T. Wong, *Adv. Mater.*, 2006, **18**, 1051-1054.
50. B. Chen, L. Wang, F. Zapata, G. Qian and E. B. Lobkovsky, *J. Am. Chem. Soc.*, 2008, **130**, 6718-6719.
51. C. Daiguebonne, N. Kerbellec, O. Guillou, J.-C. Bünzli, F. Gumy, L. Catala, T. Mallah, N. Audebrand, Y. Gérault, K. Bernot and G. Calvez, *Inorg. Chem.*, 2008, **47**, 3700-3708.
52. Z.-J. Lin, B. Xu, T.-F. Liu, M.-N. Cao, J. Lü and R. Cao, *Eur. J. Inorg. Chem.*, 2010, **2010**, 3842-3849.
53. P. J. Saines, M. Steinmann, J.-C. Tan, H. H. M. Yeung and A. K. Cheetham, *CrystEngComm*, 2013, **15**, 100-110.
54. G. E. Gomez, M. C. Bernini, E. V. Brusau, G. E. Narda, W. A. Massad and A. Labrador, *Cryst. Growth Des.*, 2013, **13**, 5249-5260.
55. G. Kickelbick, in *Hybrid Materials*, Wiley-VCH Verlag GmbH & Co. KGaA, 2007, pp. 1-48.
56. C.-Y. Sun, X.-L. Wang, X. Zhang, C. Qin, P. Li, Z.-M. Su, D.-X. Zhu, G.-G. Shan, K.-Z. Shao, H. Wu and J. Li, *Nat. Commun*, 2013, **4**.
57. P. Falcaro and S. Furukawa, *Angew. Chem. Int. Ed.*, 2012, **51**, 8431-8433.
58. M. R. N. Soares, M. J. Soares, A. J. S. Fernandes, L. Rino, F. M. Costa and T. Monteiro, *J. Mater. Chem.*, 2011, **21**, 15262-15265.
59. A. M. Kaczmarek, K. Van Hecke and R. Van Deun, *Inorg. Chem.*, 2014, **53**, 9498-9508.
60. B. W. D'Andrade and S. R. Forrest, *Adv. Mater.*, 2004, **16**, 1585-1595.
61. Y. H. Niu, M. S. Liu, J. W. Ka, J. Bardeker, M. T. Zin, R. Schofield, Y. Chi and A. K. Y. Jen, *Adv. Mater.*, 2007, **19**, 300-304.
62. H.-C. Su, H.-F. Chen, F.-C. Fang, C.-C. Liu, C.-C. Wu, K.-T. Wong, Y.-H. Liu and S.-M. Peng, *J. Am. Chem. Soc.*, 2008, **130**, 3413-3419.
63. B. Chen, Y. Yang, F. Zapata, G. Lin, G. Qian and E. B. Lobkovsky, *Adv. Mater.*, 2007, **19**, 1693-1696.
64. H. Xu, X. Rao, J. Gao, J. Yu, Z. Wang, Z. Dou, Y. Cui, Y. Yang, B. Chen and G. Qian, *Chem. Commun.*, 2012, **48**, 7377-7379.
65. Y. Yu, J.-P. Ma and Y.-B. Dong, *CrystEngComm*, 2012, **14**, 7157-7160.
66. S. Pramanik, C. Zheng, X. Zhang, T. J. Emge and J. Li, *J. Am. Chem. Soc.*, 2011, **133**, 4153-4155.
67. Y. Takashima, V. M. Martínez, S. Furukawa, M. Kondo, S. Shimomura, H. Uehara, M. Nakahama, K. Sugimoto and S. Kitagawa, *Nat. Commun*, 2011, **2**, 168.
68. P. Wu, J. Wang, Y. Li, C. He, Z. Xie and C. Duan, *Adv. Funct. Mater.*, 2011, **21**, 2788-2794.

View Article Online
DOI: 10.1039/C6RA23516F

Graphical Abstract

Luminescence, Chemical Sensing and Mechanical Properties of Crystalline Materials Based on Lanthanide-Sulfonate Coordination Polymers †

Richard F. D'Vries, [a]* German E. Gomez, [b]* Diego F. Lionello, [b] M. Cecilia Fuertes, [b] Galo J. A. A. Soler-Illia, [b] Javier Ellena. [a]

RSC Adv. **2016,**

In this work we report a series of compounds formed from lanthanide metals, 3-hydroxinaphthalene-2,7-disulfonate and 1,10-phenanthroline ligands and a complete study of relationship between the structural features with the mechanical, luminescent and sensing properties.